Journal of the Optical Society of America A
OPTICS, IMAGE SCIENCE, AND VISION

Calculation of vectorial diffraction in optical systems

JEONGMIN KIM,[1,2] YUAN WANG,[1,2] AND XIANG ZHANG[1,2,*]

[1]NSF Nanoscale Science and Engineering Center, 3112 Etcheverry Hall, University of California, Berkeley, California 94720, USA
[2]Materials Sciences Division, Lawrence Berkeley National Laboratory, 1 Cyclotron Road, Berkeley, California 94720, USA
*Corresponding author: xiang@berkeley.edu

Received 22 November 2017; revised 2 February 2018; accepted 3 February 2018; posted 5 February 2018 (Doc. ID 314083); published 12 March 2018

A vectorial diffraction theory that considers light polarization is essential to predict the performance of optical systems that have a high numerical aperture or use engineered polarization or phase. Vectorial diffraction integrals to describe light diffraction typically require boundary fields on aperture surfaces. Estimating such boundary fields can be challenging in complex systems that induce multiple depolarizations, unless vectorial ray tracing using 3 × 3 Jones matrices is employed. The tracing method, however, has not been sufficiently detailed to cover complex systems and, more importantly, seems influenced by system geometry (transmission versus reflection). Here, we provide a full tutorial on vectorial diffraction calculation in optical systems. We revisit vectorial diffraction integrals and present our approach of consistent vectorial ray tracing irrespective of the system geometry, where both electromagnetic field vectors and ray vectors are traced. Our method is demonstrated in simple optical systems to better deliver our idea, and then in a complex system where point spread function broadening by a conjugate reflector is studied.

OCIS codes: (260.1960) Diffraction theory; (180.0180) Microscopy; (080.1510) Propagation methods.

https://doi.org/10.1364/JOSAA.35.000526

1. INTRODUCTION

Vectorial diffraction theory is fundamental to the study of optical systems that have a high numerical aperture (NA) or use specific polarization, such as radial/azimuthal polarization, or engineered phase profiles. Such optical systems often appear in many important applications, including modern optical microscopy integrated with adaptive optics and point spread function (PSF) engineering, single molecule tracking, optical trapping, photolithography, and laser direct writing. The vector theory, compared with paraxial scalar diffraction theory, is rigorous because it considers polarization and nonparaxial propagation of light as well as apodization of optical systems [1]. It usually provides vectorial diffraction integrals, derived from Green's theorem as a solution of wave equations, to express a diffracted electromagnetic field [2].

The surface integrals for light diffraction require a knowledge on the integrand (or boundary) information of vectorial fields typically at the system's exit pupil. For simple focusing and imaging systems, estimating the approximate boundary fields based on geometric grounds is not difficult [3–10], from which the Debye–Wolf integral [3] is often evaluated. For systems that undergo frequent and complex depolarizations during light propagation, however, it is nontrivial to obtain boundary information unless a ray tracing concept is employed. The 3 × 3 Jones matrix formalism for tractable three-dimensional polarization tracing of electromagnetic fields was introduced over a few seminal papers [11–14] to calculate vectorial diffraction. It is not as sophisticated as software implementation-level tracing in ray optics [15,16], yet it is very effective to estimate the pupil fields. However, many important details on how to apply this method, especially for complicated systems, have not been fully addressed. For instance, many tracing examples show the sequence of Jones matrices applied, but lack information about the angle and sign used in each matrix, which is critical to understand the method. Moreover, the latest tutorial review paper [14] states that a type of system geometry (transmission versus reflection) affects a coordinate system definition to describe ray vectors, which seems to be causing some inconsistency in field tracing. We believe that not only the field vector but also the ray vector at the exit pupil must be determined by tracing (rather than set directly from the coordinate definition [14]), so that the vectorial ray tracing technique becomes consistent under any system geometry.

On the other hand, commercial optical design software such as ZEMAX and CODE V supports polarization ray tracing. Some support even vectorial diffraction calculation to a certain degree. Yet, to our knowledge, a dipole-like point source is not implemented, which is a widely accepted model of fluorescent

Corrected 12 March 2018

dye molecules in fluorescence microscopy [7]. Also, the tools lack an ideal model of a high NA objective obeying the Abbe's sine condition [17], which can be extremely useful for most application researchers who have no access to the confidential lens data of commercial microscope objectives. Thus, an accurate calculation of vectorial diffraction is limited.

In this paper, we present a complete tutorial for vectorial diffraction calculation. We first revisit several vectorial diffraction integrals with important features associated with the use of each integral. Then, we offer our tutorial on the 3 × 3 Jones matrix formalism to estimate the approximate boundary fields (both field vectors and ray vectors residing in transverse manner) needed to evaluate the diffraction integrals. Our tracing method is applicable consistently to any type of system geometry and is well-suited for complex optical systems. Diffraction calculations over several case examples of simple and complex imaging systems are demonstrated, followed by the physical interpretation of the derived PSF. We also study PSF broadening by an intermediate conjugate mirror.

2. VECTORIAL DIFFRACTION INTEGRALS

Optical diffraction is often described by an integral solution of the time-independent Helmholtz wave equation. The Stratton–Chu integral [18] derived from a vector analog of Green's theorem [2] is one for any arbitrary-shaped surface of diffraction aperture geometry as

$$\vec{E}(\vec{x}) = \frac{1}{4\pi}\iint_\Sigma [i\omega(\hat{N}\times\vec{B}_\Sigma(\vec{x}'))G + (\hat{N}\times\vec{E}_\Sigma(\vec{x}'))\times\nabla' G + (\hat{N}\cdot\vec{E}_\Sigma(\vec{x}'))\nabla' G]\mathrm{d}^2\vec{x}'. \quad \textbf{(1)}$$

It implies that an electric field $\vec{E}$, complex amplitude in the $\exp(-i\omega t)$ convention, at an observation point $\vec{x}$ in Fig. 1 is determined by boundary electric field $\vec{E}_\Sigma$ and magnetic field $\vec{B}_\Sigma$ on the diffraction aperture Σ depicted by $\vec{x}'$ (with an infinitesimal area element of $d^2\vec{x}'$), whose inward surface normal is $\hat{N}$. We use a hat symbol to denote a unit vector. $G = \exp(ikR)/R$ is the Green's function with $\vec{R} = \vec{x} - \vec{x}'$, and ∇' depicts a differential operator with respect to $\vec{x}'$. ω is a temporal angular frequency of the wave with a dispersion of $k = \omega\sqrt{\mu\epsilon}$, where k denotes the wave number, μ the permeability, and ϵ the permittivity in a medium. Many optical systems pertain to far-field diffraction ($R \gg k^{-1}$), where $\nabla' G \approx -ikG\hat{R}$. Then, with $\vec{B}_\Sigma = \sqrt{\mu\epsilon}\hat{k}_\Sigma \times \vec{E}_\Sigma$, the far-field Stratton–Chu integral can be derived as

$$\vec{E}(\vec{x}) = -\frac{ik}{4\pi}\iint_\Sigma G[(\hat{N}\cdot\hat{k}_\Sigma)\vec{E}_\Sigma - (\hat{N}\cdot\vec{E}_\Sigma)\hat{k}_\Sigma - (\vec{E}_\Sigma\cdot\hat{R})\hat{N} + (\hat{N}\cdot\hat{R})\vec{E}_\Sigma + (\hat{N}\cdot\vec{E}_\Sigma)\hat{R}]\mathrm{d}^2\vec{x}'. \quad \textbf{(2)}$$

Here, a boundary electric field and its unit propagation vector $\hat{k}_\Sigma$ are required rather than a magnetic field at the pupil, both of which are obtained by vectorial ray tracing in Section 3.

A further simplified version in widespread use is the vectorial Debye–Wolf integral [3,19], typically over spherical diffraction geometry, valid for a Fresnel number much larger than one [20], as

$$\vec{E}(\vec{x}) = -\frac{ik}{2\pi}\iint_\Omega \vec{E}_\Sigma e^{i\vec{k}_\Sigma\cdot\vec{x}}\mathrm{d}\Omega, \quad \textbf{(3)}$$

where $d\Omega = \sin\theta d\theta d\phi$ is a solid angle of $d^2\vec{x}'$. This formula can also be derived directly from Eq. (2) as $\hat{N} \approx \hat{k}_\Sigma$ in a spherical exit pupil and if the observation point $\vec{x}$ is close to the geometrical focus in Fig. 1(b), $\hat{N} \approx \hat{R}$ and $\vec{R} \approx (\vec{x}\cdot\hat{N} + f)\hat{N}$ [4]. Here, the spherically converging nature of $\vec{E}_\Sigma$ by $\exp(-ikf)/f$ at the exit pupil was added implicitly. This integral expression is physically interpreted as a superposition of plane waves [19], propagating along $\vec{k}_\Sigma$ (all pointing to the focus) with a field strength of $\vec{E}_\Sigma$, within a solid angle (Ω) of the exit pupil Σ set by numerical aperture. As a result, an axially symmetric intensity distribution is expected. Note that an optical system with a smaller Fresnel number (roughly 10 or below) requires Eq. (2) or the scaled Debye–Wolf integral [21,22], where focal shifts emerge [23,24]. Small optical aberrations $W(\theta,\phi)$ can be approximately incorporated to $\vec{E}_\Sigma$ as $\exp(ikW)$ [19] or treated more rigorously as [25]. Often, circular aperture systems allow an elimination of the azimuthal integral on ϕ under cylindrical coordinate (ρ,φ,z) of $\vec{x}$ by [3]

$$\int_{\langle 2\pi\rangle}\begin{bmatrix}\cos(m\phi)\\ \sin(m\phi)\end{bmatrix} e^{i\rho\cos(\phi-\varphi)}\mathrm{d}\phi = 2\pi i^m J_m(\rho)\begin{bmatrix}\cos(m\varphi)\\ \sin(m\varphi)\end{bmatrix}, \quad \textbf{(4)}$$

where $J_m(\rho)$ is the first kind, m order Bessel function.

We emphasize that the spherical coordinate (f,θ,ϕ) here is an alternative to the default reference Cartesian coordinate (x,y,z) to describe the pupil at $\vec{x}'$ (not the ray vector $\vec{k}_\Sigma$ as done in Refs. [12,14,26,27]). Thus, a coordinate of $(f\sin\theta\cos\phi, f\sin\theta\sin\phi, f\cos\theta)$ points at an infinitesimal area element $d^2\vec{x}'$ on the pupil that forms a solid angle of $d\Omega$, where the unit ray vector in the case of Fig. 1(b) is given as $\hat{k}_\Sigma = -\hat{x}'$; hence, $(-\sin\theta\cos\phi, -\sin\theta\sin\phi, -\cos\theta)$. In general, the ray propagation vector is to be drawn from ray tracing. More details are provided in the next section.

Other vectorial integrals include the Luneburg integral [28], valid for a planar aperture geometry normal to the optical axis ($\vec{z}$), so

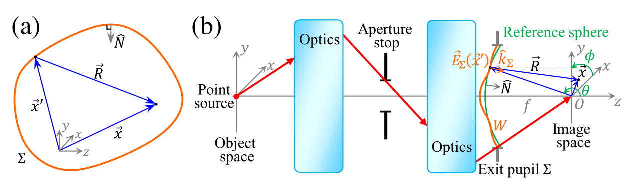

Fig. 1. (a) Schematic for diffraction integrals where boundary electromagnetic fields on $\vec{x}'$ determine a field at $\vec{x}$. The enclosed surface Σ can be practically reduced to a diffraction aperture in optical systems [2,18]. (b) Light diffraction at an aperture stop in general optical systems could be assumed to occur equivalently at the exit pupil. The field in the image space is calculated by diffraction integrals with $\vec{E}_\Sigma$ and $\hat{k}_\Sigma$ on Σ (typically the Gaussian reference sphere surface) traced from the source. (x,y,z) is the reference Cartesian coordinate and $W(\theta,\phi)$ is the wavefront error in spherical pupil coordinate (f,θ,ϕ).

$$E_{x,y}(\vec{x}) = -\frac{1}{2\pi}\iint_{\Sigma} E_{x,y}(\vec{x}')\frac{\partial G}{\partial z}\mathrm{d}^2\vec{x}',$$
$$E_z(\vec{x}) = \frac{1}{2\pi}\iint_{\Sigma}\left(E_x(\vec{x}')\frac{\partial G}{\partial x} + E_y(\vec{x}')\frac{\partial G}{\partial y}\right)\mathrm{d}^2\vec{x}', \quad \textbf{(5)}$$

where at far-field $\frac{\partial G}{\partial p} = ikG\frac{R_p}{R}$ (where $p = x, y$, and z) if $\vec{R} = R_x\hat{x} + R_y\hat{y} + R_z\hat{z}$. Thus, the far-field form of the integral for E_x and E_y is equal to the first Rayleigh–Sommerfeld diffraction integral [17]. One can find out that the same far-field integrands also result from the m-theory diffraction integral [29,30],

$$\vec{E}(\vec{x}) = \frac{1}{2\pi}\nabla\times\iint G(\hat{N}\times\vec{E}_{\Sigma})\mathrm{d}^2\vec{x}'. \quad \textbf{(6)}$$

While the Debye–Wolf integral is favorable for high NA systems with spherical pupil geometry, the Stratton–Chu and Luneburg integrals can be more suitable for optical systems with nonspherical geometry, such as axicons [31], focusing through a dielectric interface [30], and ultrathin flat optics [32,33]. The diffraction integrals can be computed directly (e.g., in MATLAB by *integral* and *integral2* functions) or indirectly [34,35]. Intensity $I(\vec{x})$, or time-averaged electric energy density, is obtained from $|\vec{E}(\vec{x})|^2$. A nonmonochromatic (or broadband) system may require a summation of each monochromatic intensity over its spectral response. Magnetic fields can be similarly calculated if interested.

3. VECTORIAL RAY TRACING

In this section, we explain how to obtain boundary field information to evaluate diffraction integrals. The electromagnetic fields and ray propagation vectors over exit pupils can be approximately estimated by polarization ray tracing using the generalized Jones matrices [12–14] listed in Table 1. Conceptually, the tracing is a sequential application of these matrices in the order that appears in an optical system. Next we provide more details on each matrix and its use.

The tracing starts from a source whose field vector (polarization) and propagation vector are known. These vectors are defined with reference to the default Cartesian coordinate (x, y, z) assigned to the optical system, such that the z-axis (parallel to the optical axis) heads in the right direction, regardless of light traveling from left to right or from right to left. For example, if a collimated source is linearly polarized along the x-axis and propagates to the positive z-axis, the initial field vector is $\vec{E} = [1; 0; 0]$ and the wave vector is $\hat{k} = [0; 0; 1]$. In general, $\vec{E}(x, y; \phi_p) = E(x, y)[\cos\phi_p; \sin\phi_p; 0]$, where ϕ_p denotes a polarization direction with respect to the x-axis, and $E(x, y)$ is a complex amplitude of the field that has to be defined if not uniform across the beam, such as a circular Gaussian beam $\exp(-(x^2 + y^2)/w_0^2)$, where w_0 denotes the beam waist. Polarization states other than a linear polarization can also be easily considered: $\vec{E} = [a; b\exp(i\delta); 0]$ for elliptical polarization, where $|a|^2 + |b|^2 = 1$ and δ is a phase delay between x/y components ($a = b = 1$, $\delta = \frac{\pi}{2}$ for circular polarization). For radial polarization, $\vec{E} = [\cos\phi_0; \sin\phi_0; 0]$, where $\phi_0 = \tan^{-1}(y/x)$ so that the field direction now depends on its lateral position of (x, y). Similarly, azimuthal polarization is expressed as $\vec{E} = [-\sin\phi_0; \cos\phi_0; 0]$. Unpolarized light can be considered indirectly by summing each intensity from the ϕ_p-polarized field incoherently over 2π rotation [3], such that $(2\pi)^{-1}\int_{\langle 2\pi\rangle}|\vec{E}(\phi_p)|^2\mathrm{d}\phi_p$.

A point source (or object) is often approximated as an electric dipole $\vec{p}$ whose far-field emission at position $\vec{r}$ is $\vec{E}(\vec{r}) = (\hat{r}\times\vec{p})\times\hat{r}$ [2]. A prefactor $k^2\exp(ikr)/(4\pi\epsilon r)$ is neglected here. An initial ray vector is then expressed as $\hat{k} = \hat{r}$. If a point object is not much smaller than the wavelength, its scattered far-field vector to start with can be obtained by the Mie theory [36]. If a spatially isotropic source is concerned (as the far-field dipole radiation is angle-dependent), intensity summed over all possible dipole orientations of 4π steradian must be considered [7]. A magnetic dipole source [2], if interested, can be treated similarly.

Table 1. 3 × 3 Jones Matrices for Vectorial Ray Tracing[a]

Coordinate rotation: $(x, y, z) \to (x_m, y_s, z)$	$\mathbb{R}_z(\phi) = \begin{bmatrix} \cos\phi & \sin\phi & 0 \\ -\sin\phi & \cos\phi & 0 \\ 0 & 0 & 1 \end{bmatrix}$	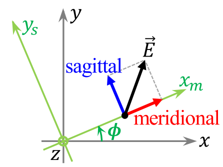
Ray refraction at a lens on the meridional plane $(x_m z)$	$\mathbb{L}(\theta) = A(\theta)\begin{bmatrix} \cos\theta & 0 & \sin\theta \\ 0 & 1 & 0 \\ -\sin\theta & 0 & \cos\theta \end{bmatrix}$	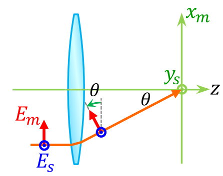
Coordinate rotation: $(x_m, y_s, z) \to (x_p, y_s, z_k)$ for p-/s- wave decomposition	$\mathbb{R}_{y_s}(\theta) = \begin{bmatrix} \cos\theta & 0 & -\sin\theta \\ 0 & 1 & 0 \\ \sin\theta & 0 & \cos\theta \end{bmatrix}$	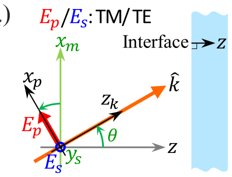
Fresnel reflection/transmission at an interface	$\mathbb{F}_R = \begin{bmatrix} r_p & 0 & 0 \\ 0 & r_s & 0 \\ 0 & 0 & 1 \end{bmatrix}$, $\mathbb{F}_T = \begin{bmatrix} t_p & 0 & 0 \\ 0 & t_s & 0 \\ 0 & 0 & 1 \end{bmatrix}$	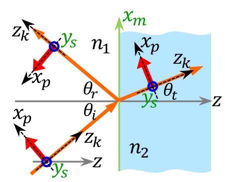
Linear polarizer	$\mathbb{P}(\psi) = \begin{bmatrix} \cos^2\psi & \sin\psi\cos\psi & 0 \\ \sin\psi\cos\psi & \sin^2\psi & 0 \\ 0 & 0 & 1 \end{bmatrix}$	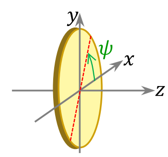
Wave plate (or phase retardation plate)	$\mathbb{W}(\delta, \psi) = \begin{bmatrix} \cos\frac{\delta}{2} + i\cos(2\psi)\sin\frac{\delta}{2} & i\sin(2\psi)\sin\frac{\delta}{2} & 0 \\ i\sin(2\psi)\sin\frac{\delta}{2} & \cos\frac{\delta}{2} - i\cos(2\psi)\sin\frac{\delta}{2} & 0 \\ 0 & 0 & 1 \end{bmatrix}$	

[a]The coordinate system is right-handed, and thus positive rotation is counterclockwise. (x, y, z) is the default Cartesian coordinate, x_m/y_s are the meridional/sagittal axes, and x_p/y_s are the p-/s-wave axes, respectively.

An optical lens is the most commonly encountered element during ray tracing. Upon refraction at the lens, an incident field is depolarized [37]. This depolarization is typically assumed to occur on only the meridional plane (see the illustration in Table 1), and thus, the field must be separated into meridional and sagittal components beforehand. This is mathematically done by the coordinate rotation matrix $\mathbb{R}_z(\phi)$, revolving about the optical axis $\hat{z}$ by ϕ (depending on the lateral position of the field vector of interest). Then the field vector is represented on the (x_m, y_s, z) basis, where the sagittal field is unaffected upon applying the ray refraction matrix $\mathbb{L}(\theta)$. Note that the ray refraction is not a coordinate rotation and the angle θ is positive for counterclockwise refraction about the sagittal axis (y_s). A nonparaxial lens may have apodization (e.g., $A(\theta) = (n_1 n_2^{-1} \cos|\theta|)^{1/2}$ in aplanatic focusing [3,9] and its inverse in aplanatic collimation), where n_1 and n_2 are refractive indices of media before and after the lens. Different forms of apodization in Herschel, Lagrange, Helmholtz, and parabolic conditions are explained in [34,38]. More rigorous tracing through a lens may include the Fresnel transmission matrix as [13], but it may be practically unnecessary. The Fresnel coefficients vary negligibly for smaller incidence angles of rays at each lens interface in both a low NA lens and a high NA objective (consisting of a group of lenses).

Reflection and transmission at an interface are considered as follows. Since the Fresnel coefficients [39] are derived for p-polarized (TM, E_p) and s-polarized (TE, E_s) waves, one needs initially to decompose the field vector as such. If the interface is planar and normal to the optical axis, the sagittal field is already a TE field. The meridional field changes to a TM field after the z-axis of its coordinate is aligned to the propagation direction (z_k) by the coordinate rotation matrix $\mathbb{R}_{y_s}(\theta)$. Then the field vector in the new (x_p, y_s, z_k) basis contains only TM/TE elements as $\vec{E} = [E_p; E_s; 0]$. After this happens, one can apply the Fresnel matrices that consist of the amplitude coefficients in a dielectric interface [39] for reflection,

$$r_p = \frac{n_2 \cos\theta_i - n_1 \cos\theta_t}{n_1 \cos\theta_t + n_2 \cos\theta_i}, \qquad r_s = \frac{n_1 \cos\theta_i - n_2 \cos\theta_t}{n_1 \cos\theta_i + n_2 \cos\theta_t}, \tag{7}$$

and transmission,

$$t_p = \frac{2n_1 \cos\theta_i}{n_1 \cos\theta_t + n_2 \cos\theta_i}, \qquad t_s = \frac{2n_1 \cos\theta_i}{n_1 \cos\theta_i + n_2 \cos\theta_t}. \tag{8}$$

The reflection coefficients for a metallic mirror can also be found at [40] (but $-r_p$ has to be used due to the handedness inversion upon reflection in their coordinate definition). As the third element of the incident field vector is zero, the (3,3) element of the Fresnel matrices has no interaction and thus could be defined otherwise [12,14]. Note that the reflected and transmitted field vectors are defined at new (x_p, y_s, z_k) bases, whose z_k axes point to reflected and transmitted ray vectors, respectively. These coordinates can be transformed back by $\mathbb{R}_{y_s}(\theta)$, most often into (x_m, y_s, z) for the subsequent tracing. If an interface (surface normal: $\hat{N}_i$) is not normal to the optical axis (that is, $|\hat{N}_i \cdot \hat{z}| \neq 1$), the above matrices may not be sufficient for tracing. A secondary coordinate rotation around $\hat{z}_k$ by θ_{z_k} may be needed after $\mathbb{R}_{y_s}(\theta)$ to assure there are correct p-/s- fields. θ_{z_k} can be decided by a geometrical requirement on the final s-wave axis as $\hat{y}_s \perp \vec{N}_i$. Otherwise, the generalized Fresnel laws [41] may be needed.

The matrices for a linear polarizer (whose azimuthal angle of the transmission axis from the $+x$ axis is ψ) and a wave plate (δ: a relative retardation between fast/slow axes; ψ: an azimuthal angle of the fast axis from the $+x$ axis) [14] are based on the reference Cartesian coordinate, and must be applied with the field vector at the same basis.

Any unequal optical path length or apodization (except at a lens) that may occur during light propagation (although not addressed by these matrices) can be incorporated by multiplying the corresponding phase or amplitude term (see Section 4.A).

We emphasize that the angles, ϕ and θ, in the Jones matrices are defined during ray tracing and the relation of these angles with spherical pupil coordinate (f, θ, ϕ) is found after the tracing. Also, the same sequence of matrices used to trace a field vector traces its ray vector while keeping $\vec{k} \cdot \vec{E} = 0$ throughout tracing (not demonstrated before), which is later related to the spherical coordinate when evaluating diffraction integrals. We do not set ray directions directly with the spherical coordinate (without tracing) as in the latest tutorial review [14]. Our way of vectorial ray tracing is consonant with any type of system geometry: transmission, reflection, or both.

It should be noted that the tracing method presented here holds for limited situations. The light source (or object) should be an on-axis, in-focus point source or a collimated source with no field angle. Any thick lens or objective lens is simplified as a thin lens with a spherically refracting surface, unlike the geometrical ray tracing in commercial software. These restrictions, however, in general do not diminish the effectiveness of estimating the PSF of optical systems. Also, a small deviation from ideal sources, such as defocused objects, laterally displaced objects, and collimated beams with field angles, could be treated by properly added aberration terms under the shift invariance assumption [26,27]. Thus, those unideal sources could still be traced as if they are ideal.

The use of symbolic calculation in computation software (MATLAB, Mathematica, etc.) makes vectorial ray tracing much more convenient as a number of matrix multiplication increase.

4. EXAMPLES

We demonstrate vectorial ray tracing and calculation of vectorial diffraction for several optical systems of practical interest.

A. High NA Focusing through a Dielectric Interface

Focusing light through index-mismatched media as shown in Fig. 2(a) is common in microscopy and optical trapping. It is important to know an axial PSF in those applications. We derive axial response when a collimated, uniform input field $\vec{E}_i = [\cos\phi_p; \sin\phi_p; 0]$ that is linearly polarized along ϕ_p with $\hat{k}_i = [0; 0; 1]$ is focused by an aplanatic objective modeled as a spherical aplanatic surface. To use the Stratton–Chu and Luneburg integrals evaluated at the dielectric interface located

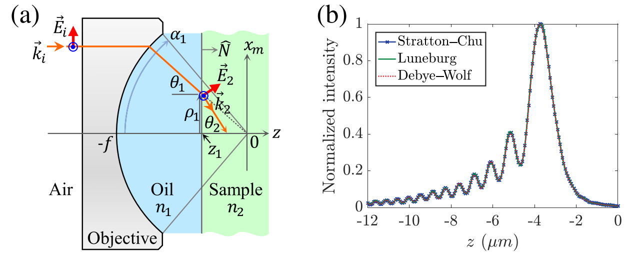

Fig. 2. (a) Schematic of aplanatic focusing through a dielectric interface on a meridional plane (NA $= n_1 \sin\alpha_1 = 1.4$, $\lambda_0 = 488$ nm (vacuum), $n_1 = 1.522$, $n_2 = 1.337$, and $f = 1.8$ mm). Meridional/sagittal fields are marked by red arrows and blue concentric circles, respectively. (b) Comparison of axial intensity when $z_1 = -20$ μm for x-polarized, uniformly incident light.

at z_1 (rather than at the exit pupil of the objective), we need an approximate boundary field at z_1^+ (right after z_1 toward the origin), which is traced as

$$\vec{E}_2 = \mathbb{R}_z^{-1}(\phi_0)\mathbb{R}_{y_s}(\theta_2)\mathbb{F}_T\mathbb{R}_{y_s}(-\theta_1)C_p\mathbb{L}(-\theta_1)\mathbb{R}_z(\phi_0)\vec{E}_i$$
$$= (n_1^{-1}\cos\theta_1)^{\frac{1}{2}}C_p \times \begin{bmatrix} t_p\cos\theta_2\cos^2\phi_0 + t_s\sin^2\phi_0 & (t_p\cos\theta_2 - t_s)\cos\phi_0\sin\phi_0 \\ (t_p\cos\theta_2 - t_s)\cos\phi_0\sin\phi_0 & t_p\cos\theta_2\sin^2\phi_0 + t_s\cos^2\phi_0 \\ t_p\sin\theta_2\cos\phi_0 & t_p\sin\theta_2\sin\phi_0 \end{bmatrix} \times \begin{bmatrix} \cos\phi_p \\ \sin\phi_p \end{bmatrix},$$
$$\hat{k}_2 \propto \mathbb{R}_z^{-1}(\phi_0)\mathbb{R}_{y_s}(\theta_2)\mathbb{F}_T\mathbb{R}_{y_s}(-\theta_1)\mathbb{L}(-\theta_1)\mathbb{R}_z(\phi_0)\hat{k}_i$$
$$\propto [-\sin\theta_2\cos\phi_0; -\sin\theta_2\sin\phi_0; \cos\theta_2], \tag{9}$$

where ϕ_0 denotes an azimuthal angle by the (x, y) location of the initial field vector, θ_1 the ray refraction at the objective lens, and θ_2 the refraction angle at the interface with t_p and t_s in Eq. (8). The matrix $\mathbb{R}_z$ separates the incident field to meridional/sagittal fields as illustrated in Fig. 2(a), from which the clockwise ray refraction $\mathbb{L}(-\theta_1)$, including the apodization of $\sqrt{1/n_1 \cdot \cos\theta_1}$, is applied. The ray propagation in n_1 medium (k_1: wave number) from the refracting surface of the objective to z_1^- adds a complex factor $C_p = f(|z_1|\cos^{-1}\theta_1)^{-1}\exp[ik_1(f + z_1\cos^{-1}\theta_1)]$. The exponent describes the optical phase difference. $f(|z_1|\cos^{-1}\theta_1)^{-1}$ accounts for apodization for the converging spherical wave on the interface [42]. The incident TE/TM components at the interface are found by $\mathbb{R}_{y_s}(-\theta_1)$ and the Fresnel-transmitted field by $\mathbb{F}_T$ changes its basis from (x_p, y_s, z_k) back to (x, y, z) by $\mathbb{R}_z^{-1}(\phi_0)\mathbb{R}_{y_s}(\theta_2)$. Note that the ray vector $\hat{k}_2$ is traced with the identical matrix sequence although $\mathbb{F}_T$ could be omitted. One can check $\hat{k}_2 \cdot \vec{E}_2 = 0$ satisfying the physics of transverse light.

Then the traced field Eq. (9) is plugged to the far-field Stratton–Chu integral in Eq. (2) where $\hat{N} = [0; 0; 1]$ and $d^2\vec{x}' = \rho_1 d\rho_1 d\phi_1$ in the cylindrical coordinate (ρ_1, ϕ_1, z_1) at the interface with $\rho_1 = |z_1|\tan\theta_1$ where $\theta_1 \in [0, \alpha_1]$. As the axial PSF along the optical axis is independent of the incident polarization direction, we set $\phi_p = 0$ to leave E_x alone as nonzero,

$$E_x(z) = -\frac{ik_2}{4\pi}\int_o^{2\pi}\int_0^a \frac{e^{ik_2R}}{R}\left[\left(\frac{R_z}{R} + \cos\theta_2\right)E_{2,x} + \left(\frac{R_x}{R} + \sin\theta_2\cos\phi_0\right)E_{2,z}\right]\rho_1 d\rho_1 d\phi_1, \tag{10}$$

where $k_2 = n_2\lambda_0$ is a wavenumber in n_2 medium, $a = |z_1|\tan\alpha_1$, $\vec{R} = -\rho_1\cos\phi_1\hat{x} - \rho_1\sin\phi_1\hat{y} + (z - z_1)\hat{z}$, $\theta_2 = \sin^{-1}(n_1/n_2\sin\theta_1)$ from Snell's law, and $\phi_0 = \phi_1$. Solving the azimuthal integral analytically leads to the axial field as

$$E(z) = -\frac{ik_2}{4}\int_0^a C_p\sqrt{\frac{\cos\theta_1}{n_1}}\frac{e^{ik_2R}}{R}\left[\left(\frac{z - z_1}{R} + \cos\theta_2\right)\times(t_p\cos\theta_2 + t_s) + \left(-\frac{\rho_1}{R} + \sin\theta_2\right)t_p\sin\theta_2\right]\rho_1 d\rho_1, \tag{11}$$

where $R = [\rho_1^2 + (z - z_1)^2]^{1/2}$, and θ_1, θ_2, C_p, t_p, and t_s are functions of ρ_1. The integral interval in Eq. (11) is related directly to θ_1 not θ_2, thus valid even when θ_1 exceeds the critical angle [43]. Axial field $E_{2,z}$ contributes less under the smaller index-mismatch, owing to $(-\rho_1/R + \sin\theta_2) \approx 0$.

A similar approach using the Luneburg and m-theory integrals was reported in [30,44] but recently corrected [42]. A Debye–Wolf approach was studied in [22], where the diffraction integral is evaluated at the spherical exit pupil, and for stratified media at high Fresnel numbers in [10,12,45]. We numerically compared our Stratton–Chu axial intensity for an oil/water interface with Luneburg and Debye–Wolf results at 1.4 NA and $z_1 = -20$ μm. As shown in Fig. 2(b), three normalized intensity profiles are well overlapped. The Stratton–Chu and Luneburg methods evaluated at the interface are more direct in deriving the focal field and work well at this high NA, but can fail if NA is small or z_1 is close to the origin as pointed out in [30,43].

Generally, a field incident to the back focal plane of the objective lens is tailored upon applications in terms of polarization, phase, and apodization. $\vec{E}_i$ needs to be defined accordingly. Various possible polarization states were described in Section 3. An engineered phase $\Phi(\theta, \phi)$ can be added to $\vec{E}_i$ by $\exp(i\Phi)$, which includes a helical phase $\exp(im\phi_0)$ for generating vortex beams where m is the orbital angular momentum index. It is also straightforward to consider phase rings or annular apertures, associated with proper piecewise integrals over polar angle θ_1. A Gaussian beam (or apodization) of $\exp(-r^2/w_0^2)$ is also related to the polar angle by $r = n_1 f\sin\theta_1$ in aplanatic focusing above.

B. PSF in High NA Microscopic Imaging

We demonstrate vectorial diffraction calculation for two simple microscopic imaging systems. First, we analyze a typical imaging system comprising an objective and a tube lens in Fig. 3, whose exit pupil is assumed to be right after the tube lens. In fact, it may be located at other place with a different diameter, yet boundary fields are still equally traced up to a constant factor. The exit pupil field for an on-axis, in-focus dipole object is traced as

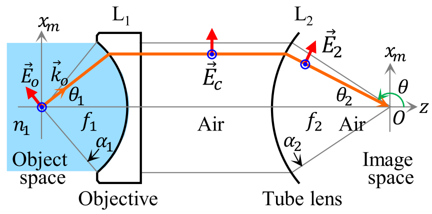

Fig. 3. Schematic of microscopic imaging of an electric dipole $\vec{p}$ emitting an object field of $\vec{E}_o = (\hat{k}_o \times \vec{p}) \times \hat{k}_o$. All the lenses are assumed aplanatic. Red arrows and blue concentric circles indicate meridional and sagittal fields, respectively.

$$\vec{E}_2 = \mathbb{R}_z^{-1}(\phi_o)\mathbb{L}_2(-\theta_2)\mathbb{L}_1(-\theta_1)\mathbb{R}_z(\phi_o)\vec{E}_o = \sqrt{n_1 \cos\theta_2 \cos^{-1}\theta_1}$$
$$\times \begin{bmatrix} p_x(\cos\theta_1 \cos\theta_2 \cos^2\phi_o + \sin^2\phi_o) + p_y(\cos\theta_1 \cos\theta_2 - 1)\cos\phi_o \sin\phi_o - p_z \sin\theta_1 \cos\theta_2 \cos\phi_o \\ p_x(\cos\theta_1 \cos\theta_2 - 1)\cos\phi_o \sin\phi_o + p_y(\cos\theta_1 \cos\theta_2 \sin^2\phi_o + \cos^2\phi_o) - p_z \sin\theta_1 \cos\theta_2 \sin\phi_o \\ p_x \cos\theta_1 \sin\theta_2 \cos\phi_o + p_y \cos\theta_1 \sin\theta_2 \sin\phi_o - p_z \sin\theta_1 \sin\theta_2 \end{bmatrix},$$
$$\hat{k}_2 \propto \mathbb{R}_z^{-1}(\phi_o)\mathbb{L}_2(-\theta_2)\mathbb{L}_1(-\theta_1)\mathbb{R}_z(\phi_o)\hat{k}_o, \qquad \textbf{(12)}$$

where the clockwise ray refraction at both lenses requires the same minus signs in $\mathbb{L}$, and $\theta_1 \in [0, \alpha_1]$, $\theta_2 \in [0, \alpha_2]$ with aplanatic apodization $\sqrt{n_1 \cos\theta_2 \cos^{-1}\theta_1}$. In [13,46], different signs seem applied, but no detail is explained. For a typical low NA tube lens, $\cos\theta_2 \approx 1$ and $\sin\theta_2 \approx 0$. A constant phase $\exp(-ikf)$ induced by each lens was neglected in the tracing. While in light focusing the meridional/sagittal planes for each collimated field vector were set by the lateral location of the field, here they are specified by the direction of each ray vector from the point source, $\hat{k}_o = [\sin\theta_1 \cos\phi_o; \sin\theta_1 \sin\phi_o; \cos\theta_1]$, and thus $\mathbb{R}_z(\phi_o)$ was applied. One can check that $\mathbb{R}_{y_s}(\theta_1)\mathbb{R}_z(\phi_o)\vec{E}_o$ leads to $E_{z_k} = 0$ as expected, and the collimated field $\vec{E}_c = \mathbb{R}_z^{-1}(\phi_o)\mathbb{L}_1(-\theta_1)\mathbb{R}_z(\phi_o)\vec{E}_o$ agrees with [5] where derived otherwise. Also, the ray vector traced as $\hat{k}_2 = [-\sin\theta_2 \cos\phi_o, -\sin\theta_2 \sin\phi_o; \cos\theta_2]$ exhibits geometrically correct signs (i.e., $\hat{k}_2 = [-;-;+]$ for $\hat{k}_o = [+;+;+]$), plus $\hat{k}_2 \cdot \vec{E}_2 = 0$. If $\theta_1 = \theta_2$, $\vec{E}_2 = [E_{ox}; E_{oy}; -E_{oz}]$, which is geometrically true.

Plugging the traced field, Eq. (12), to the Debye–Wolf integral, Eq. (3), which is valid in most microscopic imaging situations, the image field at a cylindrical observation point (ρ, φ, z) with Eq. (4) is drawn as

$$\vec{E} = \pi \begin{bmatrix} U_0^{(1)} + U_2^{(1)}\cos(2\varphi) & U_2^{(1)}\sin(2\varphi) & 2iU_1^{(1)}\cos\varphi \\ U_2^{(1)}\sin(2\varphi) & U_0^{(1)} - U_2^{(1)}\cos(2\varphi) & 2iU_1^{(1)}\sin\varphi \\ -2iU_1^{(2)}\cos\varphi & -2iU_1^{(2)}\sin\varphi & -2U_0^{(2)} \end{bmatrix} \vec{p}, \qquad \textbf{(13)}$$

where

$$U_p^{(q)} = -\frac{ik_2}{2\pi}\int_0^{\alpha_2} \sqrt{\frac{n_1 \cos\theta_2}{\cos\theta_1}} F_p^{(q)} J_p(k_2\rho \sin\theta_2)$$
$$\times \exp(ik_2 z \cos\theta_2) \sin\theta_2 \mathrm{d}\theta_2 \qquad \textbf{(14)}$$

with

$$F_0^{(1)} = 1 + \cos\theta_1 \cos\theta_2, \qquad F_0^{(2)} = \sin\theta_1 \sin\theta_2,$$
$$F_1^{(1)} = \sin\theta_1 \cos\theta_2, \qquad F_1^{(2)} = \cos\theta_1 \sin\theta_2,$$
$$F_2^{(1)} = 1 - \cos\theta_1 \cos\theta_2. \qquad \textbf{(15)}$$

Here, the original Debye–Wolf integral coordinate (θ, ϕ) was transformed to (θ_2, ϕ_o), whose angles appeared during tracing, by $\theta = \pi - \theta_2$ and $\phi = \phi_o$ (*i.e.*, $\int_{\pi-\alpha_2}^{\pi} \mathrm{d}\theta \int_0^{2\pi} \mathrm{d}\phi = \int_0^{\alpha_2} \mathrm{d}\theta_2 \int_0^{2\pi} \mathrm{d}\phi_o$). The image half-cone angle α_2 is linked with the object half-cone angle α_1 by lateral magnification $M = f_2/f_1 = n_1 \sin\alpha_1 / \sin\alpha_2$.

Note that smaller image space NA ($\alpha_2 \approx 0$) induces insignificant depolarization through the tube lens, leading to negligible axial fields due to $U_0^{(2)} \approx 0$, $U_1^{(2)} \approx 0$. Also negligible is the tube lens apodization $\sqrt{\cos\theta_2} \approx 1$. For such a paraxial tube lens, the field at the back focal plane of the objective, approximated as $\vec{E}_c$, can be directly Fourier-transformed to derive PSF for simplicity [7]. For an isotropic point object (or equivalently a freely rotating dipole molecule), integrating the above intensity $|\vec{E}|^2$ over all the orientations (4π sr.) of $\vec{p}$ [7] yields intensity PSF proportional to $|U_0^{(1)}|^2 + 2|U_1^{(1)}|^2 + |U_2^{(1)}|^2 + 2|U_0^{(2)}|^2 + 2|U_1^{(2)}|^2$. Other practical situations on the orientation of $\vec{p}$ are discussed in brightfield [5], fluorescence [7,47], and multiphoton fluorescence [47] microscopy.

Next, a microscopic imaging system may consist of other interesting optical elements such as a linear polarizer [7,46] and a special phase/polarization element [48]. Here, we exemplify an imaging system with a detector polarizer (or analyzer) in Fig. 4. We first show how to use the Jones matrices to obtain the field vector and the wavevector at the exit pupil assumed right after the L_4 lens. The collimated field right before the polarizer for a dipole object that emits $\vec{E}_o$ along $\hat{k}_o$ is

$$\vec{E}_c = \mathbb{R}_z^{-1}(\pi + \phi_o)\mathbb{L}_3(-\theta_2)\mathbb{R}_z(\pi + \phi_o)$$
$$\times \mathbb{R}_z^{-1}(\phi_o)\mathbb{L}_2(-\theta_2)\mathbb{L}_1(-\theta_1)\mathbb{R}_z(\phi_o)\vec{E}_o, \qquad \textbf{(16)}$$

or more simply $\vec{E}_c = \mathbb{R}_z^{-1}(\phi_o)\mathbb{L}_3(\theta_2)\mathbb{L}_2(-\theta_2)\mathbb{L}_1(-\theta_1)$ $\mathbb{R}_z(\phi_o)\vec{E}_o$. Note the opposite θ_2 sign of $\mathbb{L}_3$ between the two possible ways, depending on how meridional/sagittal planes right before the L_3 lens are set by $\mathbb{R}_z$. This collimated field is linked to the prior collimated field before the L_2 lens by

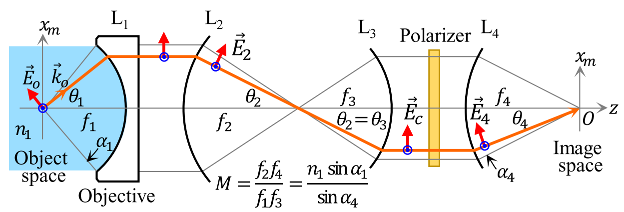

Fig. 4. Schematic of microscopic imaging of an electric dipole object through a linear polarizer.

an identity matrix $\mathbb{I} = \mathbb{R}_z^{-1}(\pi+\phi_o)\mathbb{L}_3(-\theta_2)\mathbb{R}_z(\pi+\phi_o)\mathbb{R}_z^{-1}(\phi_o)\mathbb{L}_2(-\theta_2)\mathbb{R}_z(\phi_o)$, hence pointing to the same field and propagation directions, although its field location differs azimuthally by π. Continuing ray tracing up to the exit pupil is done as

$$\vec{E}_4 = \mathbb{R}_z^{-1}(\pi+\phi_o)\mathbb{L}_4(-\theta_4)\mathbb{R}_z(\pi+\phi_o)\mathbb{P}(\psi)\vec{E}_c. \quad (17)$$

The same sequence of the matrices gives the ray vector at the exit pupil as $\hat{k}_4 = [\sin\theta_4 \cos\phi_o; \sin\theta_4 \sin\phi_o; \cos\theta_4]$, as geometrically expected. Beware of matching the basis of $\vec{E}_c$ to (x, y, z) to apply the polarizer $\mathbb{P}(\psi)$.

With the above traced field, the Debye–Wolf integral in Eq. (3) can be evaluated. Again, transforming integral coordinate (θ, ϕ) to (θ_4, ϕ_o) by $\theta = \pi - \theta_4$ and $\phi = \pi + \phi_o$, the electric field near the focal region for the vertical analyzer $(\psi = \frac{\pi}{2})$ is formulated as

$$\vec{E} = \frac{\pi}{4}\begin{bmatrix} p_x(U_0^{(1)} - U_4^{(1)}\cos(4\varphi)) + p_y(U_2^{(1)}\sin(2\varphi) - U_4^{(1)}\sin(4\varphi)) + p_z(iU_1^{(1)}\cos\varphi + iU_3^{(1)}\cos(3\varphi)) \\ p_x(U_2^{(2)}\sin(2\varphi) - U_4^{(1)}\sin(4\varphi)) + p_y(U_0^{(2)} - U_2^{(3)}\cos(2\varphi) + U_4^{(1)}\cos(4\varphi)) + p_z(-iU_1^{(2)}\sin\varphi + iU_3^{(1)}\sin(3\varphi)) \\ p_x(iU_1^{(3)}\cos\varphi + iU_3^{(2)}\cos(3\varphi)) + p_y(-iU_1^{(4)}\sin\varphi + iU_3^{(2)}\sin(3\varphi)) + p_z(U_0^{(3)} + U_2^{(4)}\cos(2\varphi)) \end{bmatrix}, \quad (18)$$

where

$$U_p^{(q)} = -\frac{ik_4}{2\pi}\int_0^{\alpha_4}\sqrt{\frac{n_1\cos\theta_4}{\cos\theta_1}}F_p^{(q)}J_p(k_4\rho\sin\theta_4) \times \exp(ik_4 z\cos\theta_4)\sin\theta_4 d\theta_4 \quad (19)$$

with

$$\begin{aligned} F_0^{(1)} &= F_4^{(1)} = (1-\cos\theta_1)(1-\cos\theta_4), \\ F_0^{(2)} &= 3 + \cos\theta_1 + \cos\theta_4 + 3\cos\theta_1\cos\theta_4, \\ F_0^{(3)} &= F_2^{(4)} = 4\sin\theta_1\sin\theta_4, \\ F_1^{(1)} &= F_3^{(1)} = 2\sin\theta_1(1-\cos\theta_4), \\ F_1^{(2)} &= 2\sin\theta_1(1+3\cos\theta_4), \\ F_1^{(3)} &= F_3^{(2)} = 2(1-\cos\theta_1)\sin\theta_4, \\ F_1^{(4)} &= 2(1+3\cos\theta_1)\sin\theta_4, \\ F_2^{(1)} &= 2(1+\cos\theta_1)(1-\cos\theta_4), \\ F_2^{(2)} &= 2(1-\cos\theta_1)(1+\cos\theta_4), \\ F_2^{(3)} &= 4(1-\cos\theta_1\cos\theta_4). \end{aligned} \quad (20)$$

Here, $k_4 (= n_4\lambda_0)$ denotes a wavenumber in image space ($n_4 = 1$ if in air). This derivation is valid for both low and high NA regime of the L_4 lens. In many microscopy applications where practically $\alpha_4 \approx 0$, the field is dominated when $\psi = \frac{\pi}{2}$ by $E_y \propto p_x U_2^{(2)}\sin(2\varphi) + p_y[U_0^{(2)} - U_2^{(3)}\cos(2\varphi)] - ip_z U_1^{(2)}\sin\varphi$ where $U_2^{(2)} \approx U_2^{(3)}$. Thus, intensity PSF for an isotropic point object can be approximately

$$I = |U_0^{(2)}|^2 + |U_1^{(2)}|^2\sin^2\varphi - 2\Re\{U_0^{(2)}U_2^{(3)*}\}\cos(2\varphi) + |U_2^{(3)}|^2, \quad (21)$$

where $\Re$ takes the real part. Here, the first term is a primary that resulted from p_y (oriented to the polarizer axis). The second term originated from p_z is the next dominant and makes the overall intensity profile vertically elongated. This anisotropic PSF, stretched to the polarizer axis ψ, stems from the polarizer-induced rotational asymmetry of the field distribution at the exit pupil. For a paraxial L_4 lens, a simplified derivation is found at [7].

We measured PSFs using fluorescent beads (F8789, Invitrogen) to compare with theoretical PSFs derived here. A diluted bead solution was dried on a plasma-etched coverslip and mounted on a microscope slide with an antifade medium (H-1000, Vector Laboratories). The bead sample was excited by a 641-nm laser and imaged by a 1.4-NA objective (oil immersion, UPLSAPO 100×, Olympus). Tube lenses used in Figs. 3 and 4 are $f_2 = f_3 = 200$ mm and $f_4 = 250$ mm. In calculating the theoretical PSF, the fluorescence signal was assumed quasi-monochromatic at 683 nm based on the spectral responses of the bead, emission filters, and the camera (3.75 µm/pixel). The 46 nm diameter bead was assumed small enough to approximate as an electric dipole in free rotation. The calculated PSF in the image space was scaled down to the object space ($n_1 = 1.512$) by magnification M. The measured PSF in Fig. 5 agreed well with the derived PSF even under the two assumptions. The full-width at half-maximum (FWHM) averaged from 16 beads differed less than 5% from the theoretical prediction. The conventional circular paraxial PSF, $2J_1(k\mathrm{NA}x)/(k\mathrm{NA}x)$, is inaccurate.

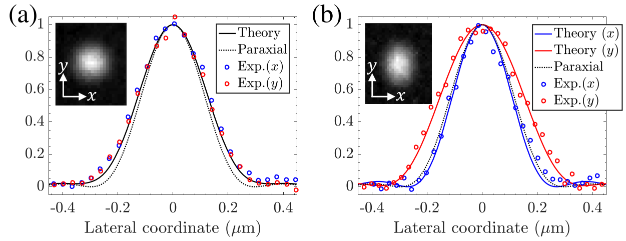

Fig. 5. Theoretical versus experimental PSF in (a) microscopic imaging (theoretical FWHM: 275.4 nm) and (b) imaging with a vertical polarizer [theoretical FWHM: 234.9 nm (x), and 329.3 nm (y)]. Two insets are images of an identical fluorescent bead at 1.4 NA. The anisotropic PSF caused by the polarizer is smaller (larger) along x (y) than the isotropic PSF in (a). The paraxial PSF, $2J_1(r)/r$, is for comparison.

C. Complex System: Microscopic Imaging with a Reflector

As an example of complex systems, we derive the PSF of an imaging system with a mirror placed in an intermediate image plane in Fig. 6. This can happen in remote focusing [49] and confocal reflection imaging. We analyze the effect of the confocal mirror on imaging PSF. For further complexity, a polarizing beam splitter (PBS) and a quarter-wave plate (QWP) is considered instead of a unpolarized beam splitter alone. We simplify the PBS as a horizontal polarizer in forward propagation and neglect a constant effect of Fresnel transmission across the field at interfaces. Similarly, in backward propagation, the PBS is treated as a vertical polarizer and the uniform reflection of the TE field at the hypotenuse surface (oblique interface) is ignored. The QWP's fast axis is azimuthally oriented by 45° from the x-axis.

Starting from the collimated field $\vec{E}_c$ before the PBS, found as Eq. (16) in the previous example, the collimated field $\vec{E}_{c2}$ right before L_5 can be traced as

$$\begin{aligned}\vec{E}_{c2} &= \mathbb{P}(90°)\mathbb{W}(90°,45°)\mathbb{R}_z^{-1}(\phi_o)\mathbb{L}_4(\theta_4)\\ &\quad\times \mathbb{R}_{y_s}^{-1}(\pi-\theta_4)\mathbb{F}_R\mathbb{R}_{y_s}(\theta_4)\mathbb{R}_z(\phi_o)\\ &\quad\times \mathbb{R}_z^{-1}(\pi+\phi_o)\mathbb{L}_4(-\theta_4)\mathbb{R}_z(\pi+\phi_o)\mathbb{W}(90°,45°)\mathbb{P}(0°)\vec{E}_c\\ &= \begin{bmatrix} 0 & 0 & 0\\ -\frac{i(r_p-r_s)}{2} & 0 & 0\\ 0 & 0 & -1\end{bmatrix}\vec{E}_c, \end{aligned} \tag{22}$$

where the Fresnel reflection coefficients for a metallic mirror (complex refractive index: n_M) [40] are given as

$$\begin{aligned} r_p &= \frac{n_M^2\cos\theta_4 - n_4\sqrt{n_M^2-n_4^2\sin^2\theta_4}}{n_M^2\cos\theta_4 + n_4\sqrt{n_M^2-n_4^2\sin^2\theta_4}},\\ r_s &= \frac{n_4\cos\theta_4-\sqrt{n_M^2-n_4^2\sin^2\theta_4}}{n_4\cos\theta_4+\sqrt{n_M^2-n_4^2\sin^2\theta_4}}. \end{aligned} \tag{23}$$

Here, only the x-component of $\vec{E}_c$ is converted to the y-polarized field $\vec{E}_{c2}$ (while its field distribution is not rotated by 90°) with a factor of $-i(r_p-r_s)/2$. This factor becomes $-i$ for a perfect mirror ($r_p=1, r_s=-1$). Also, $\hat{k}_{c2}=-\hat{k}_c=[0;0;-1]$ implied by Eq. (22) shows the correct direction of backward propagation. One can check that the x-component of the backward field right after the QWP has a prefactor of $-(r_p+r_s)/2$, thus not being completely zero unless with a perfect mirror. Note that the (x_m, y_s, z) basis is rotated to (x_p, y_s, z_k) by $\mathbb{R}_{y_s}(\theta_4)$ and returned back by $\mathbb{R}_{y_s}^{-1}(\pi-\theta_4)$ right before and after the Fresnel reflection at the mirror, respectively. The exit pupil field is finally obtained by $\vec{E}_5=\mathbb{R}_z^{-1}(\phi_o)\mathbb{L}_5(\theta_5)\mathbb{R}_z(\phi_o)\vec{E}_{c2}$ with the geometrically consistent wavevector $\hat{k}_5=[-\sin\theta_5\cos\phi_o; -\sin\theta_5\sin\phi_o; -\cos\theta_5]$ from the same Jones matrix sequence, guaranteeing that $\hat{k}_5\cdot\vec{E}_5=0$. Note that this demonstration proves the consistent tracing in our method even for the combined geometry of transmission and reflection, as opposed to the method in [14].

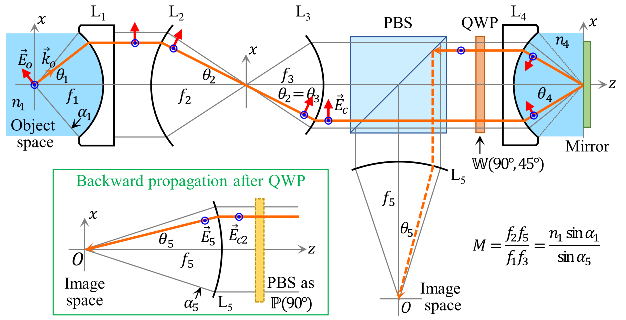

Fig. 6. Microscopic imaging with a reflector placed at an intermediate focus. In ray tracing, reflection at the PBS's hypotenuse to image space was neglected and instead a backward propagation model in the green box was considered.

If the pupil of the objective L_4 is larger than the scaled pupil of L_1 by f_3/f_2 [that is, $f_4\mathrm{NA}_4 > f_1\mathrm{NA}_1\cdot f_3/f_2$ (free from vignetting [50])], the PSF is governed by NA_1. Then the Debye–Wolf integral evaluated at the circular exit pupil, with $\theta=\theta_5$ and $\phi=\phi_o$, results in an analytical PSF as

$$\vec{E}=\frac{\pi}{4}\begin{bmatrix} p_x(U_2^{(3)}\sin(2\varphi)+U_4^{(1)}\sin(4\varphi))+p_y(U_0^{(1)}-U_4^{(1)}\cos(4\varphi))+p_z(-iU_1^{(1)}\sin\varphi+iU_3^{(1)}\sin(3\varphi))\\ p_x(U_0^{(2)}+U_2^{(1)}\cos(2\varphi)-U_4^{(1)}\cos(4\varphi))+p_y(U_2^{(2)}\sin(2\varphi)-U_4^{(1)}\sin(4\varphi))+p_z(iU_1^{(2)}\cos\varphi-iU_3^{(1)}\cos(3\varphi))\\ p_x(iU_1^{(4)}\sin\varphi+iU_3^{(2)}\sin(3\varphi))+p_y(-iU_1^{(3)}\cos\varphi-iU_3^{(2)}\cos(3\varphi))+p_z(-U_2^{(4)}\sin(2\varphi)) \end{bmatrix}, \tag{24}$$

where

$$\begin{aligned} U_p^{(q)} &= -\frac{ik_5}{2\pi}\int_0^{\alpha_5}\sqrt{\frac{n_1\cos\theta_5}{\cos\theta_1}}\frac{i(r_s-r_p)}{2}F_p^{(q)}J_p(k_5\rho\sin\theta_5)\\ &\quad\times\exp(-ik_5z\cos\theta_5)\sin\theta_5 d\theta_5 \end{aligned} \tag{25}$$

with

$$\begin{aligned} F_0^{(1)} &= F_4^{(1)} = (1-\cos\theta_1)(1-\cos\theta_5), \\ F_0^{(2)} &= 1+3\cos\theta_1+3\cos\theta_5+\cos\theta_1\cos\theta_5, \\ F_1^{(1)} &= F_3^{(1)} = 2\sin\theta_1(1-\cos\theta_5), \\ F_1^{(2)} &= 2\sin\theta_1(3+\cos\theta_5), \\ F_1^{(3)} &= F_3^{(2)} = 2(1-\cos\theta_1)\sin\theta_5, \\ F_1^{(4)} &= 2(3+\cos\theta_1)\sin\theta_5, \\ F_2^{(1)} &= 4(\cos\theta_5-\cos\theta_1), \\ F_2^{(2)} &= 2(1-\cos\theta_1)(1+\cos\theta_5), \\ F_2^{(3)} &= 2(1+\cos\theta_1)(1-\cos\theta_5), \\ F_2^{(4)} &= 4\sin\theta_1\sin\theta_5, \end{aligned} \tag{26}$$

where $\theta_1 = \sin^{-1}(M/n_1 \cdot \sin\theta_5)$ with a total magnification of M and $\theta_4 = \sin^{-1}(f_5/f_4/n_4 \cdot \sin\theta_5)$.

A typical small image NA ($\alpha_5 \approx 0$) yields an y-dominant field $E_y \propto p_x[U_0^{(2)} + U_2^{(1)}\cos(2\varphi)] + p_y U_2^{(2)}\sin(2\varphi) + ip_z U_1^{(2)}\cos\varphi$. Thus, the intensity PSF for an isotropic point object is approximately, with $U_2^{(1)} \approx U_2^{(2)}$,

$$\begin{aligned} I = &|U_0^{(2)}|^2 + |U_1^{(2)}|^2\cos^2\varphi \\ &+ 2\Re\{U_0^{(2)}U_2^{(1)*}\}\cos(2\varphi) + |U_2^{(1)}|^2, \end{aligned} \tag{27}$$

which is similar to Eq. (21) but this time is a horizontally elongated PSF. This anisotropy is attributed to a rotationally asymmetric field distribution formed by the PBS effectively as the horizontal polarizer $\mathbb{P}(0°)$ in the forward propagation. In the case of a perfect reflector, this field distribution $\vec{E}_c$ is maintained to $\vec{E}_{c2}$ [by Eq. (22) up to a constant phase of $-i$] and thus Eqs. (18) and (21) are still the valid PSF after their azimuthal adjustment by $\varphi \mapsto \varphi - (\frac{\pi}{2} - \psi)$ where $\psi = 0°$. A non-perfect (or real) mirror, however, adds apodization and wavefront errors by $-i(r_p - r_s)/2$ in Eq. (25).

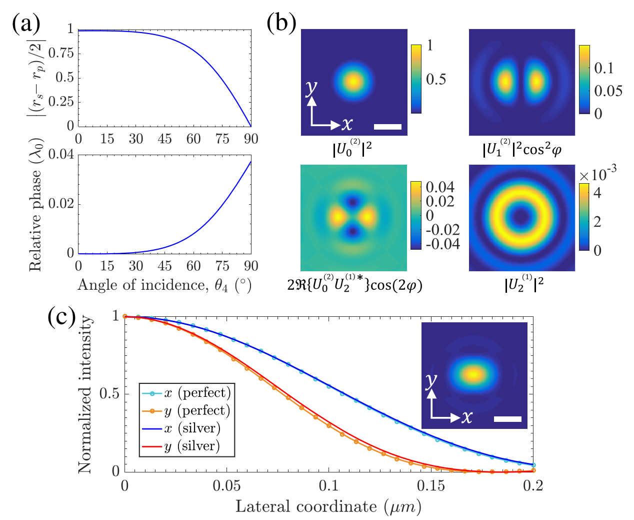

Fig. 7. Theoretical PSF with a metallic reflector at intermediate focus. (a) Amplitude and phase of $(r_s - r_p)/2$ in a silver mirror ($n_M = 0.0409 + 2.676i$, oil $n_4 = 1.525$, $\lambda_0 = 450$ nm) included in the PSF model. (b) Each intensity term of PSF in Eq. (27) at 1.4 NA. The top two distributions mainly influence the anisotropic PSF shown in the inset in (c). (c) PSF cross-sections for perfect and silver mirrors. Scale bars are 200 nm.

We numerically examined the mirror effect when $\theta_4 = \theta_1$ (satisfied if $n_4 f_4 = n_1 f_1 \cdot f_3/f_2$) and $f_5 = 200$ mm. In Fig. 7(a), the silver mirror starts to attenuate its reflected field noticeably for incident angles greater than 45° while negligibly adding a wavefront error compared to the 1/4 wave (peak-to-valley) criterion of diffraction limit. This modified apodization increased the PSF's FWHM at 1.4 NA ($n_1 = 1.525$) by 2.9% (x) and 0.6% (y) in Fig. 7(c). At 1.45 NA, the FWHM was increased by 4.0% along the x axis. The mirror-induced PSF broadening was smaller at longer wavelengths. Other common metallic mirrors (aluminum and gold) similarly modified apodization at the visible spectra, and thus will influence PSF to the same minor extent. We also checked the PSF broadening when the PBS/QWP was replaced by a unpolarized beam splitter. This layout with a silver mirror at $\lambda_0 = 450$ nm resulted in a rotationally isotropic PSF with a FWHM increase of 4.1% (5.3%) at 1.4 (1.45) NA compared to the scenario when a perfect mirror is assumed. Overall, one may ignore the effect of such reflectors on PSF in most imaging applications.

5. CONCLUSION

We presented a systematic method to calculate vectorial diffraction. We revisited vectorial diffraction integrals and provided a complete tutorial of vectorial ray tracing using the generalized Jones matrix formalism to trace electromagnetic fields throughout optical systems. Unlike the previous vectorial ray tracing approach, our method traces both field vector and ray vector as the boundary condition of vectorial diffraction integrals, which makes coordinate definitions and vectorial ray tracing consistent with any type of system geometry.

In our demonstration, we showed how to calculate a PSF in high NA focusing through index-mismatched media using the Stratton–Chu integral, followed by a comparison of axial PSF with the previous study using the Luneburg and Debye–Wolf integrals. Then we derived PSFs in standard and polarized microscopic imaging and confirmed their accuracy by experimental PSFs of fluorescent beads. We also formulated the PSF of a microscopic imaging system with a planar reflector placed at a conjugate focus, whose complicated depolarizations are hard to trace without the matrix method. The metallic reflector attenuates the field strength of high NA portion and thus slightly enlarges PSF.

The generalized calculation procedure of vectorial diffraction demonstrated here can be applied to optical systems of any complexity. The method is compatible with a source field of any polarization and amplitude/phase distribution and with any aperture geometry of systems such as annular apertures. The subject system across diverse research areas could consist of not only classical lens or polarization components, but also modern optical elements such as micro-axicons and metasurface-enabled flat optics.

Funding. Gordon and Betty Moore Foundation; Samsung.

REFERENCES

1. C. J. R. Sheppard and H. J. Matthews, "Imaging in high-aperture optical systems," J. Opt. Soc. Am. A **4**, 1354–1360 (1987).
2. J. D. Jackson, *Classical Electrodynamics*, 3rd ed. (Wiley, 1999).
3. B. Richards and E. Wolf, "Electromagnetic diffraction in optical systems. II. Structure of the image field in an aplanatic system," Proc. R. Soc. London A **253**, 358–379 (1959).
4. C. J. R. Sheppard, A. Choudhury, and J. Gannaway, "Electromagnetic field near focus of wide-angular lens and mirror systems," IEE J. Microwaves Opt. Acoust. **1**, 129–132 (1977).
5. C. J. R. Sheppard and T. Wilson, "The image of a single point in microscopes of large numerical aperture," Proc. R. Soc. London, Ser. A **379**, 145–158 (1982).
6. T. D. Visser and S. H. Wiersma, "Spherical aberration and the electromagnetic field in high-aperture systems," J. Opt. Soc. Am. A **8**, 1404–1410 (1991).
7. C. J. R. Sheppard and P. Török, "An electromagnetic theory of imaging in fluorescence microscopy, and imaging in polarization fluorescence microscopy," Bioimaging **5**, 205–218 (1997).
8. T. Wilson, R. Juškaitis, and P. Higdon, "The imaging of dielectric point scatterers in conventional and confocal polarisation microscopes," Opt. Commun. **141**, 298–313 (1997).
9. L. Novotny and B. Hecht, *Principles of Nano-Optics* (Cambridge University, 2006).
10. A. S. van de Nes, L. Billy, S. F. Pereira, and J. J. M. Braat, "Calculation of the vectorial field distribution in a stratified focal region of a high numerical aperture imaging system," Opt. Express **12**, 1281–1293 (2004).
11. R. A. Chipman, "Mechanics of polarization ray tracing," Opt. Eng. **34**, 1636–1645 (1995).
12. P. Török, P. Varga, Z. Laczik, and G. R. Booker, "Electromagnetic diffraction of light focused through a planar interface between materials of mismatched refractive indices: an integral representation," J. Opt. Soc. Am. A **12**, 325–332 (1995).
13. P. Török, P. Higdon, and T. Wilson, "On the general properties of polarised light conventional and confocal microscopes," Opt. Commun. **148**, 300–315 (1998).
14. M. R. Foreman and P. Török, "Computational methods in vectorial imaging," J. Mod. Opt. **58**, 339–364 (2011).
15. G. Yun, K. Crabtree, and R. A. Chipman, "Three-dimensional polarization ray-tracing calculus I: definition and diattenuation," Appl. Opt. **50**, 2855–2865 (2011).
16. G. Yun, S. C. McClain, and R. A. Chipman, "Three-dimensional polarization ray-tracing calculus II: retardance," Appl. Opt. **50**, 2866–2874 (2011).
17. M. Born and E. Wolf, *Principles of Optics*, 7th ed. (Cambridge University, 1999).
18. J. A. Stratton and L. J. Chu, "Diffraction theory of electromagnetic waves," Phys. Rev. **56**, 99–107 (1939).
19. E. Wolf, "Electromagnetic diffraction in optical systems. I. An integral representation of the image field," Proc. R. Soc. London A **253**, 349–357 (1959).
20. E. Wolf and Y. Li, "Conditions for the validity of the Debye integral representation of focused fields," Opt. Commun. **39**, 205–210 (1981).
21. Y. Li and E. Wolf, "Three-dimensional intensity distribution near the focus in systems of different Fresnel numbers," J. Opt. Soc. Am. A **1**, 801–808 (1984).
22. P. Török, "Focusing of electromagnetic waves through a dielectric interface by lenses of finite Fresnel number," J. Opt. Soc. Am. A **15**, 3009–3015 (1998).
23. Y. Li, "Focal shifts in diffracted converging electromagnetic waves. I. Kirchhoff theory," J. Opt. Soc. Am. A **22**, 68–76 (2005).
24. Y. Li, "Focal shifts in diffracted converging electromagnetic waves. II. Rayleigh theory," J. Opt. Soc. Am. A **22**, 77–83 (2005).
25. R. Kant, "An analytical solution of vector diffraction for focusing optical systems with Seidel aberrations," J. Mod. Opt. **40**, 2293–2310 (1993).
26. P. R. T. Munro and P. Török, "Vectorial, high-numerical-aperture study of phase-contrast microscopes," J. Opt. Soc. Am. A **21**, 1714–1723 (2004).
27. P. R. T. Munro and P. Török, "Calculation of the image of an arbitrary vectorial electromagnetic field," Opt. Express **15**, 9293–9307 (2007).
28. B. B. Baker and E. T. Copson, *The Mathematical Theory of Huygens' Principle*, 3rd ed. (AMS Chelsea Publishing, 1987).
29. B. Karczewski and E. Wolf, "Comparison of three theories of electromagnetic diffraction at an aperture. Part I: coherence matrices," J. Opt. Soc. Am. **56**, 1207–1214 (1966).
30. S. H. Wiersma, P. Török, T. D. Visser, and P. Varga, "Comparison of different theories for focusing through a plane interface," J. Opt. Soc. Am. A **14**, 1482–1490 (1997).
31. Y. Zhang, L. Wang, and C. Zheng, "Vector propagation of radially polarized Gaussian beams diffracted by an axicon," J. Opt. Soc. Am. A **22**, 2542–2546 (2005).
32. F. Aieta, P. Genevet, M. A. Kats, N. Yu, R. Blanchard, Z. Gaburro, and F. Capasso, "Aberration-free ultrathin flat lenses and axicons at telecom wavelengths based on plasmonic metasurfaces," Nano Lett. **12**, 4932–4936 (2012).
33. M. Khorasaninejad, W. T. Chen, R. C. Devlin, J. Oh, A. Y. Zhu, and F. Capasso, "Metalenses at visible wavelengths: diffraction-limited focusing and subwavelength resolution imaging," Science **352**, 1190–1194 (2016).
34. J. J. Stamnes, *Waves in Focal Regions: Propagation, Diffraction, and Focusing of Light, Sound, and Water Waves* (Adam Hilger, 1986).
35. R. Kant, "An analytical solution of vector diffraction for focusing optical systems," J. Mod. Opt. **40**, 337–347 (1993).
36. P. Török, P. Higdon, R. Juškaitis, and T. Wilson, "Optimising the image contrast of conventional and confocal optical microscopes imaging finite sized spherical gold scatterers," Opt. Commun. **155**, 335–341 (1998).
37. S. Inoué, "Studies on depolarization of light at microscope lens surfaces," Exp. Cell Res. **3**, 199–208 (1952).
38. M. Gu, *Advanced Optical Imaging Theory* (Springer-Verlag, 2000).
39. E. Hecht, *Optics*, 4th ed. (Addison-Wesley, 2002).
40. J. Peatross and M. Ware, *Physics of Light and Optics* (2015), available at http://optics.byu.edu/.
41. M. A. Dupertuis, B. Acklin, and M. Proctor, "Generalization of complex Snell–Descartes and Fresnel laws," J. Opt. Soc. Am. A **11**, 1159–1166 (1994).
42. J. Kim, Y. Wang, and X. Zhang, "Comment on 'Comparison of different theories for focusing through a plane interface'," J. Opt. Soc. Am. A (in press).
43. C. J. R. Sheppard and P. Torok, "Effects of specimen refractive index on confocal imaging," J. Microsc. **185**, 366–374 (1997).
44. S. H. Wiersma and T. D. Visser, "Defocusing of a converging electromagnetic wave by a plane dielectric interface," J. Opt. Soc. Am. A **13**, 320–325 (1996).
45. P. Török and P. Varga, "Electromagnetic diffraction of light focused through a stratified medium," Appl. Opt. **36**, 2305–2312 (1997).
46. P. Török, P. D. Higdon, and T. Wilson, "Theory for confocal and conventional microscopes imaging small dielectric scatterers," J. Mod. Opt. **45**, 1681–1698 (1998).
47. P. D. Higdon, P. Török, and T. Wilson, "Imaging properties of high aperture multiphoton fluorescence scanning optical microscopes," J. Microsc. **193**, 127–141 (1999).
48. M. P. Backlund, A. Arbabi, P. N. Petrov, E. Arbabi, S. Saurabh, A. Faraon, and W. E. Moerner, "Removing orientation-induced localization biases in single-molecule microscopy using a broadband metasurface mask," Nat. Photonics **10**, 459–462 (2016).
49. E. J. Botcherby, R. Juskaitis, M. J. Booth, and T. Wilson, "An optical technique for remote focusing in microscopy," Opt. Commun. **281**, 880–887 (2008).
50. P. Török and T. Wilson, "Rigorous theory for axial resolution in confocal microscopes," Opt. Commun. **137**, 127–135 (1997).